

Experiments on the magnetorotational instability in helical magnetic fields

Frank Stefani¹, Thomas Gundrum¹, Gunter Gerbeth¹, Günther Rüdiger², Jacek Szklarski², and Rainer Hollerbach³

¹ Forschungszentrum Dresden-Rossendorf, P.O. Box 510119, D-01314 Dresden, Germany

² Astrophysikalisches Institut Potsdam, An der Sternwarte 16, D-14482 Potsdam, Germany

³ Department of Applied Mathematics, University of Leeds, Leeds, LS2 9JT, United Kingdom

Abstract. The magnetorotational instability (MRI) plays a key role in the formation of stars and black holes, by enabling outward angular momentum transport in accretion disks. The use of combined axial and azimuthal magnetic fields allows the investigation of this effect in liquid metal flows at moderate Reynolds and Hartmann numbers. A variety of experimental results is presented showing evidence for the occurrence of the MRI in a Taylor-Couette flow using the liquid metal alloy GaInSn.

PACS numbers: 47.20.-k, 47.65.+a, 95.30.Qd

Submitted to: *New J. Phys.*

1. Introduction

The existence of compact astrophysical objects relies on the fact that they accumulate matter from their surroundings. Typically, the matter around stars and black holes has organized itself into so-called accretion disks. Before falling into the central object the rotating gas must be slowed down. Unlike the energy, which can be radiated away, the angular momentum of the rotating gas can only be transported within the disk. The molecular viscosity of the gas is much too small to explain the angular momentum transport needed to account for the accretion rates of stars and black holes. Turbulent flows would suffice, but the onset of turbulence would appear to be forbidden by the Rayleigh criterion, stating that differentially rotating fluids become unstable only if their angular momentum decreases outward [1]. This obviously does not hold true for Keplerian flows, whose angular momentum increases as the square root of the radius. It is widely believed [2] that finite amplitude instabilities would ultimately destabilize even such linearly stable flows, but recent experiments on rotating flows, with carefully controlled axial boundary conditions, seem to indicate the opposite [3].

This intriguing discussion about the possible role of finite amplitude instabilities was circumvented by Balbus and Hawley in a seminal 1991 paper [4]. They showed that even weak magnetic fields dramatically alter the stability criterion of rotating flows. In fact, the basic idea of this “magnetorotational instability” (MRI) was not completely new. As early as 1959, Velikhov had demonstrated that an axial magnetic field could destabilize a Rayleigh-stable Taylor-Couette (TC) flow, provided the angular velocity decreases with radius [5]. This result was later confirmed by Chandrasekhar [6], so the MRI may also be referred to as the “Velikhov-Chandrasekhar instability.”

For a TC flow driven by differentially rotating inner and outer cylinders, the relevant stability boundaries are sketched in Fig. 1. If the ratio $\mu := \Omega_o/\Omega_i$ of the outer and inner cylinders’ rotation rates is less than the squared ratio $(r_i/r_o)^2$ of the inner and outer cylinders’ radii, then according to the Rayleigh criterion the flow is always unstable (at least in the inviscid limit). In contrast, if μ is greater than one, then according to the Velikhov-Chandrasekhar criterion the flow is stable. The MRI occurs in the parameter regime between these two lines, where the flow is hydrodynamically stable, but magnetohydrodynamically unstable. And returning to the astrophysical application that Balbus and Hawley had in mind, we note that Keplerian flows are precisely in this regime.

As a result of this astrophysical importance of the MRI, there is considerable interest in achieving it in laboratory experiments as well [7]. For the classical Velikhov-Chandrasekhar (and also Balbus-Hawley) configuration, with the externally applied magnetic field being purely axial, these attempts have not entirely succeeded so far. The underlying reason for this is that an azimuthal field, which is necessary for the MRI to proceed, must then be produced from the applied axial field by the rotation of the flow. This is only possible in flows with sufficiently large magnetic Reynolds numbers Rm (defined as the product of magnetic permeability, electrical conductivity,

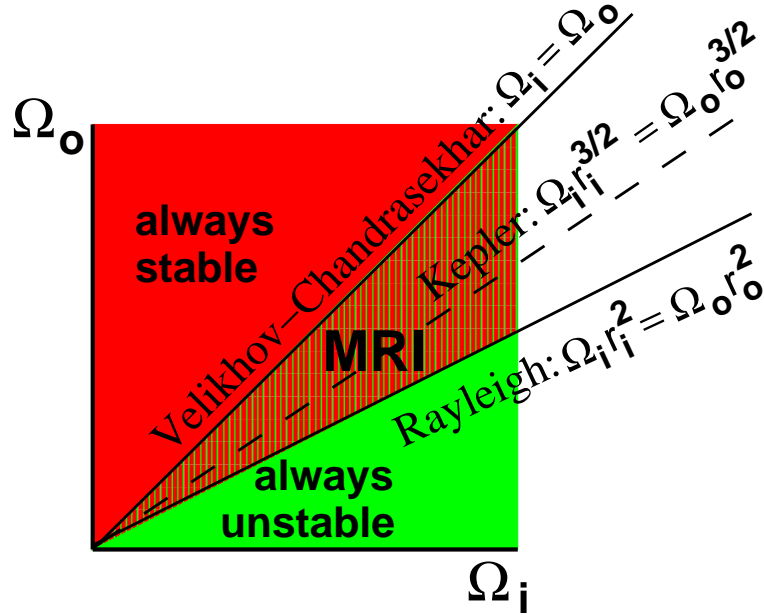


Figure 1. Stability diagram of a Taylor-Couette flow with and without magnetic fields. Whereas the hydrodynamic Rayleigh line separates flows with increasing and decreasing *angular momentum*, the magnetohydrodynamic Velikhov-Chandrasekhar line separates flows with increasing and decreasing *angular velocity*. The dashed line indicates a Keplerian profile, having angular velocity $\Omega \sim r^{-3/2}$ decreasing, but angular momentum $\Omega r^2 \sim r^{1/2}$ increasing. (This particular example is for $r_i/r_o = \sqrt{1/2}$.)

length scale and mean velocity of the flow). Such large magnetic Reynolds numbers are very difficult to achieve, typically only in sodium-cooled fast-breeder reactors or in special dynamo experiments [8]. The only MRI experiment to achieve such large values of Rm is that of Lathrop’s group [9], who obtained an instability whose dependence on Rm , as well as on the field strength, is indeed rather similar, if perhaps not identical to, the classical MRI. However, this instability arose from an already highly turbulent background flow, contradicting the original goal of identifying the MRI as the *first* instability on a laminar background flow.

Given that it is so difficult to produce the required azimuthal field by the flow, why not simply replace the induction process by externally applying an azimuthal magnetic field as well? This question was addressed in a recent paper by Hollerbach and Rüdiger [10], who showed that the MRI is then possible with far smaller Reynolds (Re) and Hartmann (Ha) numbers. This new type of MRI, sometimes called the “helical MRI” [11] or the “inductionless MRI” [12], is currently the subject of intense discussions in the literature [11, 12, 13, 14, 15]. Indeed, the astrophysical relevance of magnetorotational instabilities in helical magnetic fields is still a matter of some controversy, dating back to an early dispute between Knobloch [16, 17] and Hawley and Balbus [18].

Notwithstanding this ongoing discussion, the dramatic decrease of the critical Reynolds number for the onset of the MRI in helical magnetic fields, as compared

with the case of a purely axial field, makes this new type of MRI very attractive for experimental studies. Initial results of the experiment “PROMISE” (*Potsdam ROssendorf Magnetic InStability Experiment*) were published recently [19, 20]. In this paper we report further results. In particular, we document how the classical Taylor vortex flow for $\mu = 0$ changes to a very slowly traveling wave under the influence of helical magnetic fields.

2. The Experimental Facility

The PROMISE facility, shown in Fig. 2, is a cylindrical Taylor-Couette cell with externally imposed axial and azimuthal (i.e., helical) magnetic fields. Its primary component is a cylindrical copper vessel V, fixed on a precision turntable T via an aluminum spacer D. The inner wall of this vessel is 10 mm thick, extending in radius from 22 to 32 mm; the outer wall is 15 mm thick, extending from 80 to 95 mm. The outer wall of this vessel forms the outer cylinder of the TC cell. The inner cylinder I, also made of copper, is fixed on an upper turntable, and is then immersed into the liquid metal from above. It is 4 mm thick, extending in radius from 36 to 40 mm, leaving a 4 mm gap between it and the inner wall of the containment vessel V. The actual TC cell therefore extends in radius from 40 to 80 mm, for a gap width $d = r_o - r_i = 40$ mm. The fluid is filled to a height of 410 mm, for an aspect ratio of ~ 10 .

The fluid is the eutectic alloy $\text{Ga}^{67}\text{In}^{20.5}\text{Sn}^{12.5}$, which is liquid at room temperatures. The physical properties of GaInSn at 25 °C are as follows: density $\rho = 6.36 \times 10^3$ kg/m³, kinematic viscosity $\nu = 3.40 \times 10^{-7}$ m²/s, electrical conductivity $\sigma = 3.27 \times 10^6$ (Ω m)⁻¹. The magnetic Prandtl number is $Pm = \mu_0 \sigma \nu = 1.40 \times 10^{-6}$.

In the current experimental setup, the upper endplate of the TC cell is a plexiglass lid P, fixed to the frame F, and hence stationary. The lower endplate is simply part of the copper vessel V, and thus rotates with the outer cylinder. There is therefore a clear asymmetry in the endplates, with regard to both their rotation rates and electrical conductivities.

Hydrodynamic TC experiments are typically done using glass cylinders, which allow for very good geometrical accuracy, to within $\sim 10^{-2}$ mm [21]. We used copper cylinders here because the critical Reynolds and Hartmann numbers for the onset of the MRI are somewhat smaller with perfectly conducting boundaries than with insulating boundaries [13], suggesting that copper would be more suitable than glass or plexiglass. However, the price to pay for this is that $\sim 10^{-2}$ mm accuracy is no longer achievable when drilling and polishing a material as soft as copper. What is more, to ensure a well-defined electrical contact between the fluid and the walls, it is necessary to intensively rub the GaInSn into the copper; the resulting abrasion then limits the accuracy to no better than $\sim 10^{-1}$ mm.

The rotation frequencies of the inner and outer cylinders are measured by the Reynolds number $Re = 2\pi f_i r_i d / \nu$ and the ratio $\mu = f_o / f_i$. Typical Reynolds numbers in the experiment are $O(10^3)$, some 30 times greater than the $Re_c = 68.2$ onset of

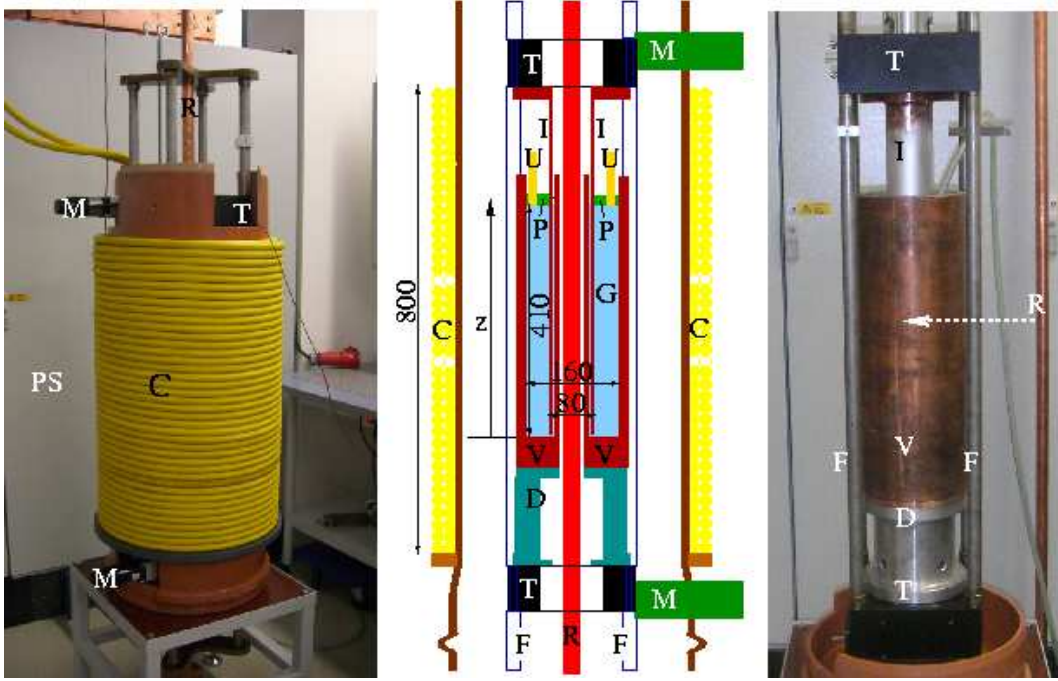


Figure 2. The left panel shows the complete PROMISE facility; the right panel shows the central module, without the coils C, and with the rod R taken out of the center. The middle panel shows a schematic sketch, with the numbers indicating lengths in mm, and the letters denoting the following: V - Copper vessel, I - Inner cylinder, G - GaInSn, U - Two ultrasonic transducers, P - Plexiglass lid, T - High precision turntables, M - Motors, F - Frame, C - Coil, R - Copper rod, PS - Power supply up to 8000 A.

nonmagnetic Taylor vortices in TC flows with $\mu = 0$ (for a radius ratio $\eta := r_i/r_o$ of 0.5). For the rotation ratio μ , we will consider both $\mu < 0.25$, for which the basic flow profile is already Rayleigh-unstable, as well as $\mu > 0.25$, for which it is Rayleigh-stable, but MRI-unstable. One of the issues then that we will particularly want to focus on is how the behavior changes as we cross the Rayleigh line $\mu = 0.25$.

Axial magnetic fields of order 10 mT are produced by a double-layer coil (C). Windings were omitted at two symmetric positions close to the middle in order to optimize the homogeneity of the field throughout the region occupied by the fluid. Currents up to 200 A are driven through this coil, achieving axial fields up to $B_z = 20.35$ mT, or in nondimensional units up to a Hartmann number $Ha := B_z(r_i d\sigma/\rho\nu)^{1/2}$ of 31.65. The azimuthal field B_ϕ , also of order 10 mT (at r_i), is generated by a current through a water-cooled copper rod (R) of radius 15 mm. The power supply for this axial current delivers up to 8000 A. In the following this current will be referred to as the “rod current.”

In nonmagnetic TC experiments the flow can be visualized and measured by a wide variety of techniques. In contrast, making measurements in liquid metal flows is non-trivial. The first measurements of axial velocities in liquid metal TC flows were by

Takeda [22], using Ultrasound Doppler Velocimetry (UDV). Applying a similar technique [23], our measuring instrumentation consists simply of two ultrasonic transducers, fixed into the upper plexiglass lid, 15 mm away from the outer copper wall, flush mounted at the interface to the GaInSn, and with special high-focus sensors having a working frequency of 4 MHz. With this instrumentation we can then measure the axial velocity v_z at the particular location $r = 65$ mm (averaged over the approximately 8 mm width of the ultrasound beam), as a function of time t and height z along the cylinder axis. The resolutions in t and z were adjustable (within limits); in most runs we used resolutions of 1.84 sec in t and 0.685 mm in z . Finally, having two transducers, on opposite sides of the TC cell, was important in order to be able to distinguish between the expected axisymmetric ($m = 0$) MRI [10, 13], and an unexpected non-axisymmetric $m = 1$ instability which arose in certain parameter regimes.

3. The Dependence on μ

3.1. Nonmagnetic results

Some preliminary experiments on the onset of nonmagnetic Taylor vortex flow (TVF) were done with a water-glycerol mixture. Thereafter we filled the vessel with the GaInSn, but continued to do nonmagnetic runs. Measuring the initial onset of TVF was unfortunately not possible, because the velocities corresponding to $Re = 68$ were too small to measure with our ultrasound technique. (The water-glycerol mixture had a considerably greater viscosity, so $Re = 68$ translates into correspondingly greater velocities there, making those measurements easier, and a useful test of the basic ultrasound technique.)

Even though obtaining the initial onset of the classical $\mu = 0$ TVF was not possible for the GaInSn, we were able to measure how the existing, super-critical TVF gradually disappears again as we increase μ beyond the Rayleigh line $\mu = 0.25$. Figure 3 shows measurements for eight different values of μ , from 0 to 0.3. The inner cylinder's frequency was fixed at $f_i = 0.1$ Hz, corresponding to $Re = 2958$; the outer cylinder's frequency was then adjusted to yield the indicated values of μ . For $\mu = 0$, the alternating red and blue stripes indicate a steady TVF with 5 pairs of rolls along the vertical axis, exactly as we would expect for a TV cell of aspect ratio 10. Increasing μ , this TVF gradually breaks up in both space and time, eventually disappearing completely. For $\mu = 0.25$ and 0.3 there is no trace of TVF; what we see instead is simply an Ekman flow driven by the top and bottom endplates. We recall that the upper lid is stationary, whereas the lower lid rotates with the outer cylinder. In both cases this drives a radially inward Ekman pumping, leading to v_z being positive/negative in the upper/lower halves of the cell [24]. Note also how these two Ekman vortices are asymmetric about the midplane, due to the stronger pumping at the upper, stationary lid. The two regions are separated by a boundary containing a jet-like radial outflow, as discussed in [25].

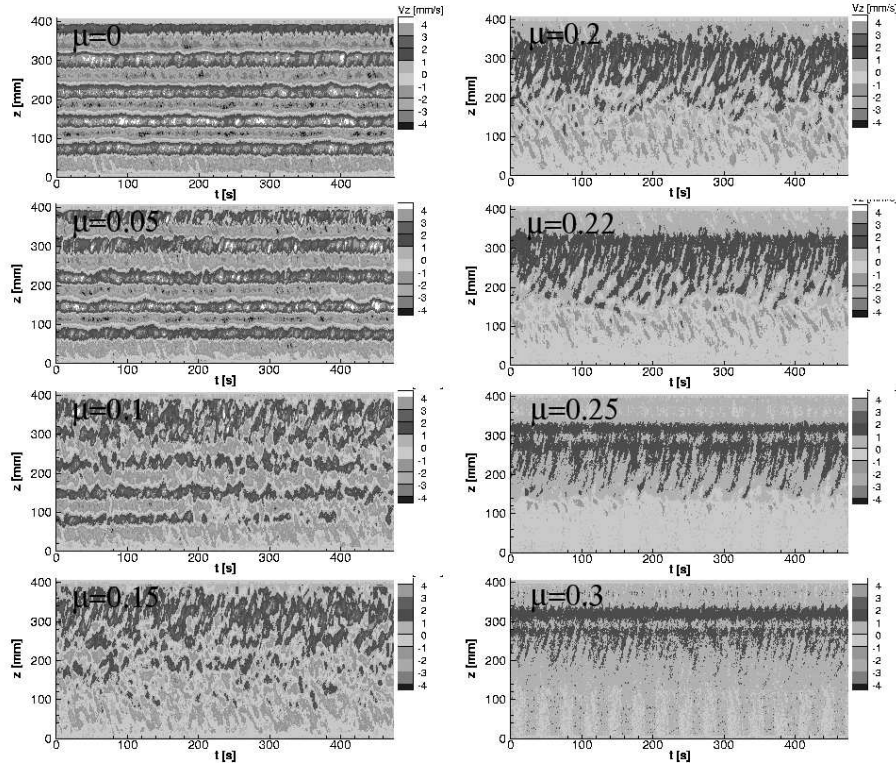


Figure 3. v_z at $r = 65$ mm, as a function of time t and height z . The inner cylinder's rotation rate is fixed at $f_i = 0.1$ Hz ($Re = 2958$); the outer cylinder's rotation rate is adjusted to yield the indicated values of $\mu = f_o/f_i$. $I_{\text{coil}} = I_{\text{rod}} = 0$, so these results are completely nonmagnetic.

3.2. $\mu = 0$, purely axial or purely azimuthal fields

Before considering the effect of helical magnetic fields, it is interesting to examine the influence of purely axial or purely azimuthal fields, neither of which yields an MRI at these small values of Re . Figure 4 shows v_z in these cases, namely a purely axial field on the left, and a purely azimuthal field on the right, and $Re = 2958$ and $\mu = 0$ for both. We note how the basic TVF structure is essentially the same as in the nonmagnetic case, apart from minor changes in strength, and a slight fluctuation in time. In subsequent sections we will see that helical fields do indeed yield rather different results, just as predicted theoretically.

3.3. Increasing μ , helical magnetic fields

Purely axial and purely azimuthal magnetic fields both have the property that $\pm z$ are identical (apart from the asymmetries introduced by the different boundary conditions on the top and bottom endplates). This is reflected in Figs. 3 and 4, which show relatively little top/bottom asymmetry. In contrast, helical magnetic fields break this reflectional symmetry, as first pointed out by Knobloch [17]. As a result of this symmetry

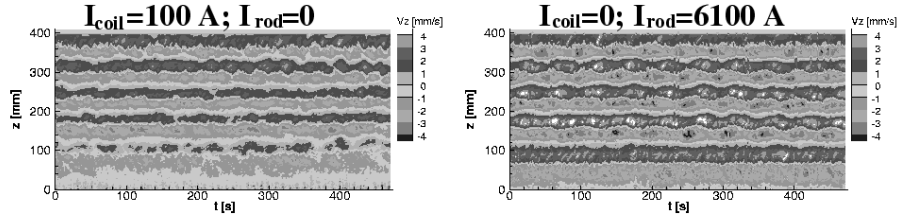


Figure 4. The left panel has a purely axial field, with $I_{\text{coil}} = 100$ A; the right panel has a purely azimuthal field, with $I_{\text{rod}} = 6100$ A. The inner cylinder rotates at $f_i = 0.1$ Hz ($Re = 2958$); the outer cylinder is stationary ($\mu = 0$).

breaking, the previously steady TVF is forced to drift in z , resulting in a traveling-wave TVF (still axisymmetric though). The direction of propagation, that is, whether the pattern drifts in the $+z$ or $-z$ directions, depends on whether the screw-sense of the magnetic field is either parallel or anti-parallel to the flow rotation. For a given helical field, the waves therefore propagate in one direction only; standing waves do not arise in this problem.

Figure 5 shows results for the helical field generated by the currents $I_{\text{coil}} = 60$ A and $I_{\text{rod}} = 6100$ A, corresponding to $Ha = 9.5$, and the ratio $\beta := B_\varphi(r_i)/B_z = 6.0$. The inner cylinder's rotation is fixed at $f_i = 0.05$ Hz, corresponding to $Re = 1479$, and the outer cylinder's rotation is again adjusted to yield the indicated values of μ . Comparing these results with the nonmagnetic results in Fig. 3, we see that the two are already different for $\mu = 0$. We now have slightly inclined red and blue stripes, indicating that the TVF rolls are no longer steady, but drift upward in time. For $\mu = 0$ the frequency of this wave is very small, around 1.6 mHz, only 3% of f_i . The frequency increases with increasing μ , reaching 9 mHz, or 18% of f_i .

We see therefore that the previously steady TVF has indeed been replaced by a unidirectionally traveling-wave TVF. Furthermore, unlike in Fig. 3, where the TVF rolls disappeared as we increased μ beyond the Rayleigh line, in this case these TVF waves continue to exist at $\mu = 0.25$ and even 0.27, gradually fading away only for $\mu = 0.3$ and 0.35. These traveling-wave instabilities beyond the Rayleigh line are precisely the theoretically predicted MRI.

It is interesting to compare the measured wave frequencies with predictions from two different numerical methods. First, we can solve the 1-dimensional linear eigenvalue problem in an axially unbounded cylinder, with perfectly conducting inner and outer boundaries [10, 26, 27]. The second method is to solve the full 2-dimensional nonlinear problem in a properly bounded cylinder, as presented in [14].

The left panel in Fig. 6 shows how the experimental Reynolds number $Re = 1479$ compares with the critical Reynolds number obtained from the 1D linear eigenvalue analysis; we see that at $\mu = 0$ the experiment is some 7 times supercritical, but at $\mu = 0.27$ it is only about twice supercritical, and at $\mu = 0.3$ it is slightly subcritical, in agreement with Fig. 5, where the wave indeed fades away between $\mu = 0.27$ and

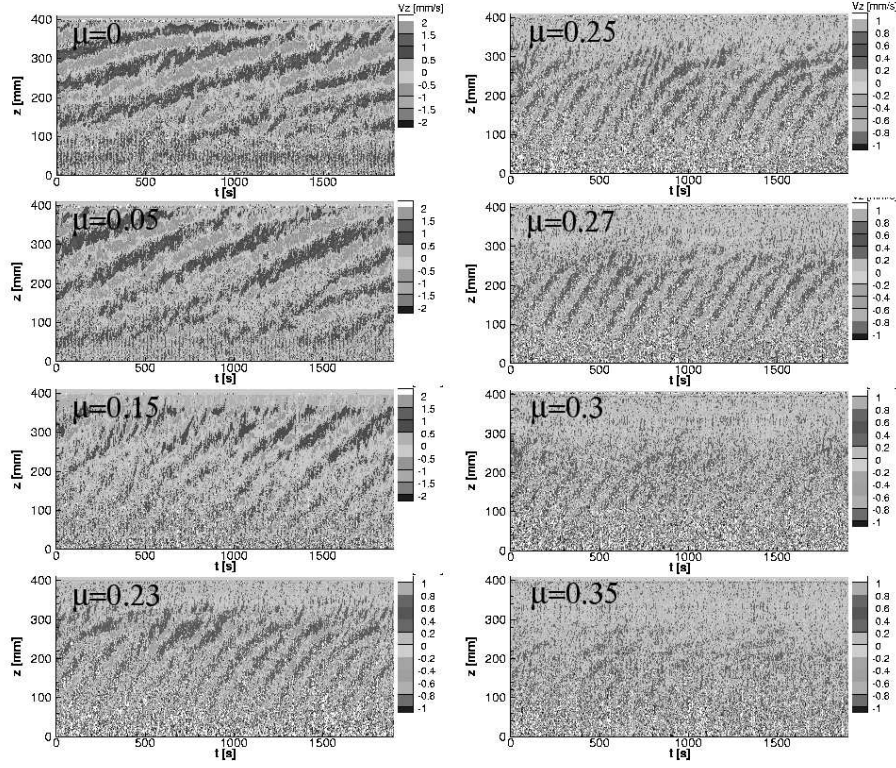


Figure 5. $I_{\text{coil}} = 60$ A, corresponding to $Ha = 9.5$; $I_{\text{rod}} = 6100$ A, corresponding to $\beta := B_{\varphi}(r_i)/B_z = 6.0$. The inner cylinder's rotation rate is fixed at $f_i = 0.05$ Hz ($Re = 1479$); the outer cylinder's is adjusted according to the indicated values of μ . Note how the frequency of the waves increases with increasing μ .

0.3. The right panel in Fig. 6 compares the measured and computed wave frequencies, normalized to f_i . The overall agreement is quite good. Note how both the measured values and the 2D simulation yield a slightly slower increase with μ than that predicted by the (more highly idealized) 1D analysis.

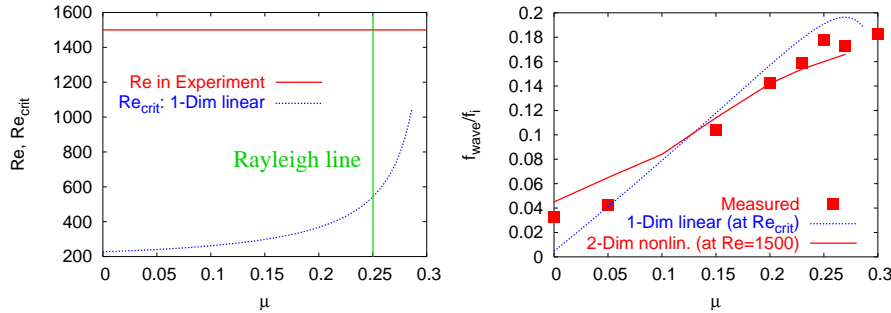


Figure 6. The left panel compares the experimental Reynolds number $Re = 1479$ with the critical value from the 1D eigenvalue problem. The right panel compares the experimental wave frequencies with results from the 1D and 2D numerical calculations.

Finally, Fig. 7 shows the detailed spatio-temporal structure of the $\mu = 0.27$ 2D simulation, and compares it with the corresponding panel from Fig. 5. The magnitudes of v_z are not quite the same, but otherwise the agreement is rather good. It is particularly gratifying to note that the waves are concentrated between $z \approx 50$ and 250 in both the experiment and the simulation, suggesting that the simulation is properly reproducing the end-effects that cause the waves to fade away at the ends. The frequencies and wavelengths are also in reasonable agreement between the two panels.

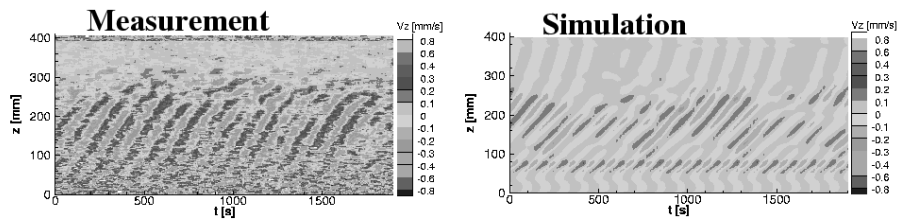


Figure 7. The left panel is the same as the $\mu = 0.27$ panel in Fig. 5., but with a moving average over 20 data points and a modified velocity scale. The right panel is from the corresponding 2D numerical simulation, also at $\mu = 0.27$, $Re = 1479$, $Ha = 9.5$ and $\beta = 6.0$.

4. Increasing B_z , for fixed B_φ

In the previous section we have considered the dependence on μ , for various magnetic field configurations. We now fix $\mu = 0.27$ ($f_i = 0.06$ Hz, $f_o = 0.0162$ Hz, $Re = 1775$), and consider the dependence on the field. We begin with Fig. 8, showing the effect of a purely azimuthal field (so similar to Fig. 4b, but now beyond the Rayleigh line, rather than at $\mu = 0$). Without a field (the left panel), the flow does not exhibit any coherent structures at all, certainly nothing like TVF cells. There is a slight modulation at the frequency f_o , probably due to geometrical imperfections of the outer cylinder, or perhaps oxides sticking to it. Switching on the azimuthal field (the right panel), these structures become somewhat more pronounced, but continue to be restricted to a very narrow region in the center of the apparatus. There is certainly nothing like the traveling-wave structures observed in Fig. 5. This is of course only to be expected, since a purely azimuthal field does not yield an MRI, at least not at such a small value of Re .

What we wish to consider next is what happens if we now gradually switch on the axial field. Once it is sufficiently strong, we would certainly expect to recover the MRI, just as in Fig. 5. If we continue increasing the axial field though, we would also expect the MRI to disappear again, since it only exists within a certain range of field strengths, but disappears if the field is either too weak or too strong. This well-known feature of the MRI was previously documented in [19]; here we substantiate it in more detail.

Figure 9 therefore shows a sequence of eight runs, all at the previous values $\mu = 0.27$, $Re = 1775$, $I_{rod} = 6000$ A, and I_{coil} increasing from 20 to 140 A as indicated. At 20 A we

still have a rather featureless flow, similar to Fig. 8 (in fact, more like the nonmagnetic left panel than the magnetic right panel). However, at 40 A we already see the same traveling-wave MRI as in Fig. 5. Increasing I_{coil} further, this mode increasingly fills the apparatus, until at 80 and 90 A it extends over almost the entire height. Finally, at 100 A this mode begins to disappear again, and by 140 A we are back to the same featureless flow we started out with.

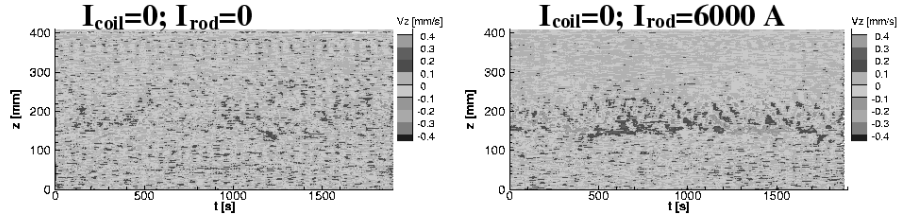


Figure 8. $\mu = 0.27$, $Re = 1775$ and $I_{\text{coil}} = 0$ for both panels; the left panel also has $I_{\text{rmrod}} = 0$, the right panel has $I_{\text{rod}} = 6000$ A. Note the absence of any TVF structures.

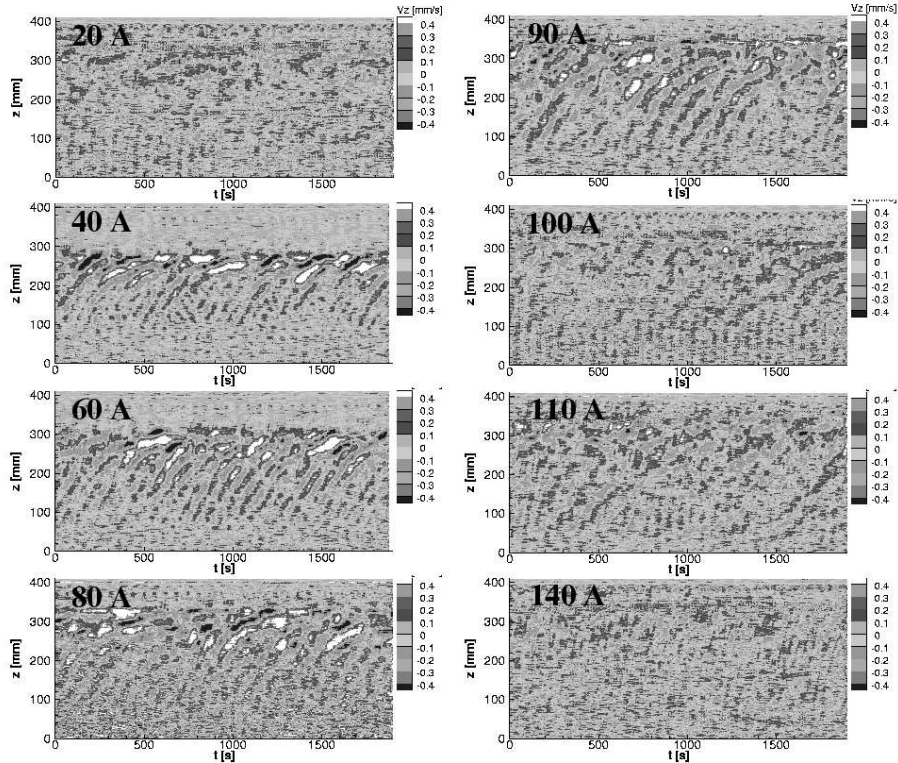


Figure 9. v_z as a function of t and z , with the rotation rates fixed at $\mu = 0.27$ and $Re = 1775$, the azimuthal field fixed at $I_{\text{rod}} = 6000$ A, and the axial field increasing from $I_{\text{coil}} = 20$ to 140 A as indicated. The traveling-wave MRI only exists for the intermediate range $I_{\text{coil}} = 40$ to 100 A.

Figures 10 and 11 show further details of the behavior at 70 A, so right in the

middle of the MRI regime in Fig. 9. In particular, Fig. 10 compares the signals from the two ultrasound transducers, and shows that these modes are indeed the same at both sensors, as they ought to be for an axisymmetric instability mode. Figure 11 also shows both sensors, but now shows the effect of suddenly switching on the field (both B_z and B_φ simultaneously). Ideally one would like to use this data to extract the linear growth rate of the instability, and compare it with the theoretical predictions. The UDV technique unfortunately cannot deliver very small values of v_z accurately enough to obtain a definite growth rate, but we can certainly observe that the MRI is fully developed 200–300 sec after switching on the field, consistent with the expected growth rate of $\sim 0.1 f_i$.

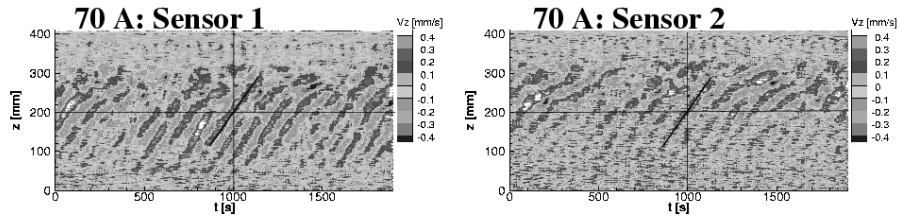


Figure 10. Measurements made by the two ultrasound sensors. The inclined bars show that the two signals are in phase, as required for an axisymmetric mode. $\mu = 0.27$, $Re = 1775$, $I_{\text{rod}} = 6000$ A, $I_{\text{coil}} = 70$ A.

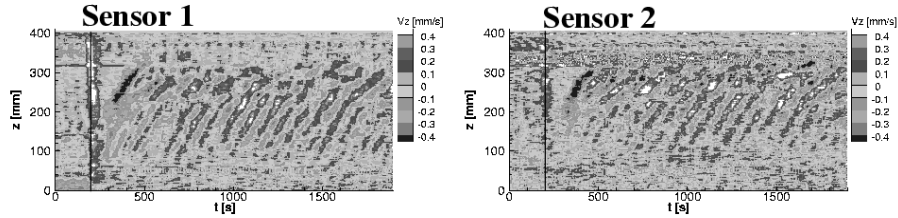


Figure 11. The field ($I_{\text{rod}} = 6000$ A, $I_{\text{coil}} = 70$ A) is suddenly switched on at $t = 200$ sec, indicated by the black lines. Some 200–300 sec later the traveling-wave MRI is essentially fully developed, consistent with the expected growth rate of around $0.1 f_i$. $\mu = 0.27$, $Re = 1775$.

Figure 12 compares the experimental results with some of the 1D numerical results [10, 26, 27]. First, the red squares and lines compare the measured frequencies with two different computed frequencies, namely at Re_{crit} , and at the experimental value $Re = 1775$. The difference between the two numerical results is fortunately small, suggesting that the frequency in the nonlinear, saturated regime (the regime the experiment is in) is most likely also close to these values. The measured frequencies are certainly in reasonable agreement with the computed ones, and in particular also exhibit a maximum around $Ha = 10$.

Next, the dotted blue line is the numerically computed linear growth rate at $Re = 1775$, and shows that (a) at this value of Re the MRI should exist between

$Ha = 5$ and 17, or $I_{\text{coil}} = 30$ and 110 A, broadly consistent with Fig. 9, and (b) the maximum growth rate, at $Ha = 11$, is $0.1f_i$, consistent with Fig. 11. Finally, the blue circles denote the measured rms values of v_z . Note how these values are greatest in the same $5 < Ha < 17$ interval where we expect the MRI (although they are also significantly different from zero outside this range).

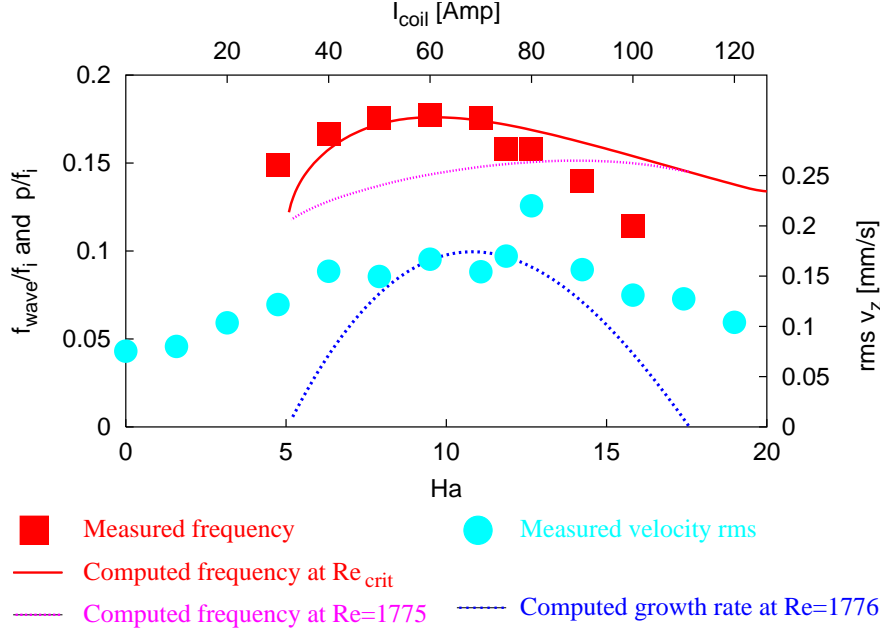


Figure 12. Various comparisons of experimental (squares and circles) and numerical (lines) results, as functions of I_{coil} , or equivalently Ha . $I_{\text{rod}} = 6000$ A, $\mu = 0.27$ and $Re = 1775$. Normalized frequencies f_{wave}/f_i and growth rates p/f_i are indicated on the left axis; rms values of v_z on the right axis.

5. An Unexpected Non-axisymmetric Mode

All of the results presented so far are in general agreement with the theoretical predictions for the axisymmetric traveling-wave MRI. In contrast, Fig. 13 shows an unexpected non-axisymmetric mode, which occurred for $f_i = 0.05$ Hz, $f_o = 0.0135$ Hz, $I_{\text{rod}} = 6720$ A, and $I_{\text{coil}} = 110$ A, or in dimensionless numbers $\mu = 0.27$, $Re = 1479$, $Ha = 17.4$ and $\beta = 3$. The two sensors are now out of phase, indicative of a non-axisymmetric mode, most likely $m = 1$. The frequency of this mode is 0.21 Hz. Such a non-axisymmetric mode is not expected as the first instability (although similar $m = 1$ instabilities are known to exist in the related Tayler instability problem [28]), but could conceivably arise as a secondary instability of the axisymmetric traveling-wave state, or could alternatively be due to a lack of perfect axisymmetry in the apparatus (e.g. due to the field induced by the I_{rod} current when it flows through the leads to the central rod). Fully understanding this non-axisymmetric mode will require further work, both experimental and numerical (i.e. extending the 2D nonlinear code to 3D).

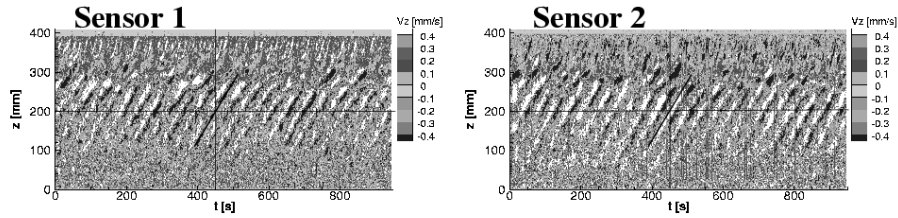


Figure 13. $\mu = 0.27$, $Re = 1479$, $I_{\text{rod}} = 6720$ A, $I_{\text{coil}} = 110$ A. The inclined bars show that the two signals are out of phase, corresponding to an $m = 1$ mode.

6. Conclusions and Future Prospects

In this work we have presented experimental results that make a strong case for the existence of a magnetorotational instability in the presence of an externally applied helical magnetic field. In particular, we showed that a unidirectionally traveling wave disturbance is excited, and continues to exist beyond the Rayleigh line. The frequency of this wave, as well as its dependence on the axial field strength, are in good agreement with 1D and 2D numerical calculations. This traveling-wave MRI differs in important ways from the classical MRI considered by Velikhov [5], Chandrasekhar [6], and Balbus and Hawley [4], but it does share the most basic features that any magnetorotational instability ought to possess, namely that it would not exist without the magnetic field, but on the other hand, is not driven by the field, but instead draws all its energy from the differential rotation. (The argument over the astrophysical relevance of helical magnetic fields for the MRI [16, 17, 18, 11] will most likely continue though.)

Regarding future experimental work, a modification of the apparatus is currently under way, to symmetrize the axial boundary conditions by using plexiglass at both ends. The use of split rings for the endplates, as suggested by [25, 29], and implemented in the (so far nonmagnetic) experiment by [3], is also planned. This should significantly reduce the Ekman circulation cells and the associated radial jet close to the midplane. We hope that the transition to the MRI will then be considerably sharper than it is in the results presented here.

There is also much numerical work that remains to be done, including a more realistic treatment of the magnetic boundary conditions, both radial and axial (copper is after all not a perfect conductor). Given the good agreement obtained so far, this is unlikely to significantly affect the results, but certainly needs to be investigated. Next, a 3D finite-cylinder code needs to be developed, to study aspects like this non-axisymmetric instability in section 5. Finally, from a general theoretical point of view, there is an urgent need to clarify the issue of convective versus absolute instabilities, which also arises in many other problems related to TC flows [30].

Acknowledgments

This work was supported by the German Leibniz Gemeinschaft, within its SAW program. We thank Heiko Kunath for technical assistance, and Markus Meyer for assistance taking some of the data. The Rossendorf group also thanks Janis Priede and Ilmars Grants for stimulating discussions.

References

- [1] Rayleigh Lord 1929 *On the dynamics of revolving fluids* Scientific papers **6** 447-453
- [2] Richard D and Zahn J-P 1999 *Astron. Astrophys.* **347** 734
- [3] Ji H, Burin M, Schartman E and Goodman J 2006 *Nature* **444** 343
- [4] Balbus S A and Hawley J F 1991 *Astrophys. J.* **376** 214
- [5] Velikhov E P 1959 *Sov. Phys. JETP* **36** 995
- [6] Chandrasekhar S 1960 *Proc. Nat. Acad. Sci.* **46** 253
- [7] Rosner R, Rüdiger G, and Bonanno A (eds) 2004 *MHD Couette Flows: Experiments and Models* AIP Conf. Proc. No. 733 (AIP, New York)
- [8] Gailitis A, Lielausis O, Platacis E, Gerbeth G and Stefani F 2002 *Rev. Mod. Phys.* **74** 973
- [9] Sisan D R, Mujica N, Tillotson W A, Huang Y M, Dorland W, Hassam A B, Antonsen T M and Lathrop D P 2004 *Phys. Rev. Lett.* **93** 114502
- [10] Hollerbach R and Rüdiger G 2005 *Phys. Rev. Lett.* **95** 124501
- [11] Liu W, Goodman J, Herron I and Ji H 2006 *Phys. Rev. E* **74** 056302
- [12] Priede J, Grants I and Gerbeth G 2006 *Preprint physics/0606122*
- [13] Rüdiger G, Hollerbach R, Schultz M and Shalybkov D A 2005 *Astron. Nachr.* **326** 409
- [14] Szklarski J and Rüdiger G 2006 *Astron. Nachr.* **327** 844
- [15] Bonanno A and Urpin V 2006 *Phys. Rev. E* **73** 066301
- [16] Knobloch E 1991 *Mon. Not. R. Astron. Soc.* **255** 25
- [17] Knobloch E 1996 *Phys. Fluids* **8** 1446
- [18] Hawley J F and Balbus S A 1992 *Astrophys. J.* **400** 595
- [19] Stefani F, Gundrum T, Gerbeth G, Rüdiger G, Schultz M, Szklarski J and Hollerbach R 2006 *Phys. Rev. Lett.* **97** 184502
- [20] Rüdiger G, Hollerbach R, Stefani F, Gundrum T, Gerbeth G and Rosner R 2006 *Astrophys. J.* **649** L145
- [21] Schultz-Grunow F 1959 *Z. Angew. Math. Mech.* **39** 101
- [22] Takeda Y, Fischer W E, Sakakibara J and Ohmura K 1993 *Phys. Rev. E* **47** 4130
- [23] Cramer A, Zhang C and Eckert S 2004 *Flow Meas. Instrum.* **15** 145
- [24] Czarny O, Serre E, Bontoux and Lueptow R M 2003 *Phys. Fluids* **15** 467
- [25] Kageyama A, Ji H, Goodman J, Chen F and Shoshan E 2004 *J. Phys. Soc. Jpn.* **73** 2424
- [26] Rüdiger G, Schultz M and D. Shalybkov 2003, *Phys. Rev. E* **67**, 046312
- [27] Stefani F and Gerbeth G 2004 In [7], p. 100
- [28] Rüdiger G, Schultz M, Shalybkov D and Hollerbach R 2006 *Preprint astro-ph/0611478*
- [29] Hollerbach R and Fournier A 2004 In [7], p. 114
- [30] Tsameret A and Steinberg V 1991 *Europhys. Lett.* **14** 331